Advances in Computational Science and Engineering
Vol. 8, 2026, pp. 22-49 (April 3, 2026)
doi:10.3934/acse.2026006

HIGH-FIDELITY FINITE ELEMENT MODELLING OF MULTI-LAYER 3D PRINTING WITH COMPLEX TOOLPATHS

Giacomo Rizzieri*[1], Liberato Ferrara[1]
and Massimiliano Cremonesi[1]

[1]Department of Civil and Environmental Engineering, Politecnico di Milano,
Piazza Leonardo da Vinci 32, 20133, Milan, Italy

(Communicated by Antonia Larese)

Abstract. Extrusion-based additive manufacturing produces objects by depositing material layer-by-layer, yet predicting geometry and structural integrity remains challenging due to complex material rheology, nozzle dynamics, and toolpath dependence. High-fidelity models can capture extrusion dynamics and the true layer shape, but have traditionally been limited to simple geometries and few layers. This work extends these simulations to multi-layer structures with complex geometries involving overhangs and twists, while automatically managing intricate G-codes. A Particle Finite Element Method (PFEM) framework is employed to handle free-surface evolution, large deformations, and the time-dependent viscoplastic behaviour of the extruded material. Two novel strategies for G-code optimization - arc-based toolpath resampling and adaptive time-step cutting - are also proposed to ensure accurate nozzle motion resolution while maintaining computationally efficient simulation time steps. Applied to virtual printing of complex objects, the framework shows when material and geometry jointly determine stability and shape fidelity, enabling optimization of additive manufacturing across polymers, bioprinting inks, clays, and cementitious materials.

1. Introduction.

Over the past decades, extrusion-based additive manufacturing, often referred to as 3D printing, has seen widespread adoption across a range of industries, including automotive and aerospace manufacturing, biomedical engineering, and construction. Initially developed for rapid prototyping, it has since evolved into a production-ready technology, enabling the fast and accurate fabrication of digital models through layer-by-layer material deposition.

A key feature of extrusion-based deposition is its versatility across a broad spectrum of materials, including polymers, glass and bio-inks, clays and cement-based composites [1]. While the mechanisms of solidification vary - glass and polymers primarily undergo thermal phase transitions, whereas bioprinting and cement-based materials rely on a combination of time-dependent rheological behaviour and chemically induced reactions - all extrusion-based processes follow the same fundamental

---

2020 *Mathematics Subject Classification.* Primary: 58F15, 58F17; Secondary: 53C35.

Key words and phrases. Extrusion-based additive manufacturing, high-fidelity simulation, Particle Finite Element Method (PFEM), G-code optimization, buildability, material rheology.

*Corresponding author: Giacomo Rizzieri.

principle: material is extruded through a nozzle in a fluid or semi-fluid state, deposited along a predetermined path, and gradually solidifies or gains mechanical strength to support subsequent layers.

As a result, extrusion-based processes face similar challenges, ranging from filament-scale defects and flow instabilities to overall poor quality or even structural failure of the printed part due to residual stresses, inadequate interlayer adhesion or insufficient material strength [9, 39, 49]. Predicting such outcomes is critically important yet remains challenging due to the complex rheological behaviour of the inks, the large number of strongly interdependent process parameters (e.g., printing speed, feed rate, nozzle geometry, stand-off distance) [34], and the fact that the optimal combination of parameters is highly dependent on the geometry and complexity of the printed part.

For these reasons, numerical modelling has gained significant interest over the past decade and is gradually becoming an essential tool for understanding and optimizing 3D printing [51, 23]. Particularly, modelling approaches can be classified into two categories based on spatial scale and dominant physical phenomena: filament-scale models, which resolve the mechanics of extrusion and deposition, and structural-scale models, which address global geometrical conformity, anisotropy, and mechanical stability of the printed part.

Filament-scale models are typically fluid-based and aim to capture the physics of material flow during injection, extrusion through the nozzle, and subsequent filament deposition. In polymer-based 3D printing, fluid-based modelling efforts primarily focus on thermoplastic behaviour and the influence of process parameters on material flow and deposition. For instance, in [42] the extrusion of a Newtonian thermoplastic ink was numerically investigated with the finite-volume-based software FLOW-3D. The Finite Volume Method (FVM) has been widely employed to study polymer melt flow, with particular emphasis on quantifying viscoelastic effects in Direct Ink Writing (DIW) [52] and Fused Filament Fabrication (FFF) [50]. Hybrid approaches combining the Finite Element Method (FEM) with streamline-based remeshing have also been proposed to model the flow of fibre-reinforced polymer melts and predict fibre orientations during printing [46]. In the field of bioprinting an Arbitrary Lagrangian–Eulerian (ALE) finite element approach was developed in [6] to assess cell viability during extrusion flow.

Building on the framework introduced by [42], a FVM-based model for cement-based material extrusion was developed in [7] and validated through comparison of simulated and experimentally measured filament cross-sections. For cement-based materials and clays, the primary objective of the simulations is to capture the non-Newtonian rheology and its interaction with process parameters, which governs the extrusion flow regime and the resulting filament geometry. In this context, the Particle Finite Element Method (PFEM) [20], an updated Lagrangian FEM formulation combined with adaptive remeshing, has proven particularly effective for simulating extrusion and single- or multi-layer filament deposition [26, 29, 31, 28]. These models have also demonstrated the ability to reproduce typical printing defects including, e.g., over- and under-extrusion, filament tearing, and slug formation [34].

Despite their high physical fidelity, filament-scale models are generally limited to simulating one or only a few deposited layers, as extending them to larger, multilayer structures rapidly becomes computationally prohibitive.

Structural-scale simulations instead typically adopt a solid-mechanics perspective, representing the progressive build-up of the printed structure through simplified yet efficient selective layer or element activation in finite element models.

For polymer-based processes, structural-scale modelling has focused on mesoscale thermal analysis and the prediction of residual stresses during cooling. A layer-by-layer activation framework in Abaqus/CAE has been proposed in [2] for modelling 3D printing with fibre-reinforced thermoplastics and accounting for material anisotropy when predicting part distortion. A meso- to macroscopic Abaqus-based framework was also developed for FDM in [4], making use of sequential element activation to capture thermally induced deformations. Further advancements were proposed in [25] for the efficient thermal simulation of FFF combining element activation with adaptive refinement, allowing element size to increase with distance from the nozzle.

For cement-based materials, full-scale simulations have focused on assessing buildability and predicting failure modes either buckling or plastic collapse. Early Abaqus-based models employing layer-wise activation were presented in [48, 49]. Subsequently, element-activation-based approaches were extended to handle more complex geometries, including printing of overhanging and branching structural components [21], non-planar geometries [18], and large-scale structures [37].

However, structural-scale models generally neglect the real extrusion dynamics, the local plastic deformations near the nozzle, and pressure build-up beneath it. Moreover, the deposited filament is often idealized using simple geometric representations - most commonly rectangular cross-sections - thereby overlooking the true filament shape resulting from the deposition process.

Advances in constitutive modelling for phase-transitioning materials, along with the growing availability of high-performance computing, CPU and GPU parallelization, and machine-learning-assisted solvers, are expected to progressively enhance extrusion-based 3D printing simulations, improving accuracy across scales and bridging the gap between fluid- and solid-based approaches.

This work contributes to that effort by demonstrating how fluid-based models can be extended to simulate structures more complex than those previously considered in the literature, while accounting for high-fidelity extrusion dynamics, including below-nozzle pressure and yielding, as well as the exact layer shape. Specifically, we present simulations of objects consisting of up to 20 layers with complex geometries that extend beyond simple rectilinear or cylindrical forms, featuring overhangs, twists, and height-varying cross-sections. This approach not only expands the range of structures addressable with high-fidelity models but also requires careful consideration of toolpath reproduction - a challenge that remains largely unexplored in these frameworks. Solid-based methods in fact, typically build the FEM model in advance from the toolpath [27] simplifying the process. Fluid-based simulations on the other hand must consider proper toolpath resolution and select appropriate time steps to accurately capture progressive material flow and nozzle motion. In this work, we propose two novel strategies for optimizing the G-code to ensure accurate toolpath reproduction in the FEM model while allowing for large simulation time steps.

We begin in Section 2 by presenting the general continuum formulation and the governing equations. Section 3 then describes the finite element discretization of the problem and introduces the Particle Finite Element Method (PFEM) [20] to handle large deformations and free-surface evolution. The PFEM, combined with tailored techniques for reproducing the 3D printing process [31, 34, 28], enables high-fidelity simulation of material extrusion. In this work, the ink is assumed to behave as a viscoplastic material undergoing progressive time-dependent structuration.

The second objective, addressed in Section 4, is to extend fluid-based 3D printing simulations to complex toolpaths. This includes careful treatment of toolpath handling and time-step selection to accurately resolve nozzle motion while maximizing computational efficiency. To this end, we propose two novel strategies: a user-controlled arc-based toolpath resampling and time-step cutting.

Finally, in Section 5, the framework is applied to simulate complex parametric geometries featuring twisting and overhangs, directly from externally generated G-code. Simulations are conducted with different material properties to investigate the influence of yield stress on the overall buildability and geometric fidelity.

2. Continuum model.

Let us assume that the extrusion material can be idealized as homogeneous, isothermal, and incompressible. This hypothesis generally holds for clays, cement-based materials, and certain types of polymers and bio-inks. The governing equations are formulated within the Arbitrary Lagrangian–Eulerian (ALE) framework, which permits the computational mesh to move independently of the material points [10]. Let Ω_t denote the evolving fluid domain over the time interval $[0, T]$. The spatial position in the current configuration is represented by $\boldsymbol{x}$, whereas $\boldsymbol{\chi}$ denotes the reference coordinates associated with the moving mesh. Under these assumptions, the balance of linear momentum and the mass continuity equation can be written as:

$$\rho \frac{d\boldsymbol{u}}{dt} = \nabla_{\boldsymbol{x}} \cdot \boldsymbol{\sigma} + \rho \boldsymbol{b} \quad \text{in } \Omega_t \times [0, T], \tag{1}$$

$$\nabla_{\boldsymbol{x}} \cdot \boldsymbol{u} = 0 \quad \text{in } \Omega_t \times [0, T], \tag{2}$$

where ρ is the (constant) density, $\boldsymbol{u} = \boldsymbol{u}(\boldsymbol{x}, t)$ is the velocity field, $p = p(\boldsymbol{x}, t)$ is the pressure field, $\boldsymbol{\sigma} = \boldsymbol{\sigma}(\boldsymbol{x}, t)$ is the Cauchy stress tensor, $\boldsymbol{b}$ is the vector of the external accelerations and $\frac{d(\bullet)}{dt} = \left.\frac{\partial(\bullet)}{\partial t}\right|_{\boldsymbol{\chi}} + \boldsymbol{c} \cdot \nabla_{\boldsymbol{x}}(\bullet)$ represents the total time derivative, with $\boldsymbol{c}$ being the convective velocity associated with the motion of the material points relative to the mesh reference system.

A suitable set of initial and boundary conditions must also be prescribed:

$$\boldsymbol{u}(\boldsymbol{x}, t = 0) = \boldsymbol{u}_0(\boldsymbol{x}) \quad \text{in } \Omega_0, \tag{3}$$

$$p(\boldsymbol{x}, t = 0) = p_0(\boldsymbol{x}) \quad \text{in } \Omega_0, \tag{4}$$

$$\boldsymbol{u}(\boldsymbol{x}, t) = \widetilde{\boldsymbol{u}}(\boldsymbol{x}, t) \quad \text{on } \Gamma_D \times (0, T), \tag{5}$$

$$\boldsymbol{\sigma} \cdot \boldsymbol{n} = \boldsymbol{h}(\boldsymbol{x}, t) \quad \text{on } \Gamma_N \times (0, T), \tag{6}$$

where $\boldsymbol{u}_0$, p_0, $\widetilde{\boldsymbol{u}}$, $\boldsymbol{h}$, are given known functions and $\boldsymbol{n}$ is the outward normal to the boundary $\Gamma_t = \partial\Omega_t$, which is subdivided into two non-overlapping subsets, Γ_D and Γ_N, such that $\Gamma_D \cup \Gamma_N = \Gamma_t$ and $\Gamma_D \cap \Gamma_N = \emptyset$.

To complete the formulation, the Cauchy stress tensor is commonly decomposed into a volumetric and a deviatoric part:

$$\boldsymbol{\sigma} = -p\boldsymbol{I} + \boldsymbol{\tau}, \tag{7}$$

where $\boldsymbol{I}$ denotes the identity tensor and $\boldsymbol{\tau}$ the deviatoric stress tensor, which can be computed after prescribing a suitable rheological law.

Many materials used in 3D printing - ranging from clays and cement-based mixtures to certain polymers and bio-inks - exhibit viscoplastic behaviour. The simplest and most widely adopted rheological model used to describe this behaviour is the Bingham model, which accounts for the presence of a yield stress. When the von Mises norm of the deviatoric stress tensor is below the yield stress, the material behaves as a rigid solid. Once this threshold is exceeded, the material yields and begins to flow. The Bingham constitutive law is expressed as:

$$\boldsymbol{\tau} = 2\mu\dot{\boldsymbol{\epsilon}} + \tau_0(t)\frac{\dot{\boldsymbol{\epsilon}}}{\|\dot{\boldsymbol{\epsilon}}\|} \qquad \text{if } \|\boldsymbol{\tau}\| > \tau_0(t), \tag{8}$$

$$\dot{\boldsymbol{\epsilon}} = \mathbf{0} \qquad \text{otherwise}, \tag{9}$$

where μ is the fluid viscosity, τ_0, as specified in the following, is the time-dependent yield stress, $\| \bullet \|$ is the von Mises norm and $\dot{\boldsymbol{\epsilon}}$ is the deviatoric strain rate tensor. To simplify the numerical solution, the model implements the Papanastasiou regularization of the Bingham law [22]:

$$\boldsymbol{\tau} = \left(2\mu + \frac{\tau_0(t)}{\|\dot{\boldsymbol{\epsilon}}\|}(1 - e^{-m\|\dot{\boldsymbol{\epsilon}}\|})\right)\dot{\boldsymbol{\epsilon}} = \mu_{app}(\dot{\boldsymbol{\epsilon}})\dot{\boldsymbol{\epsilon}}, \tag{10}$$

where m is a regularization parameter governing the quality of the exponential approximation and $\mu_{app}(\dot{\boldsymbol{\epsilon}})$ can be interpreted as an equivalent apparent viscosity.

Furthermore, many of the aforementioned materials exhibit reversible, time-dependent structural evolution immediately after deposition. This behaviour, commonly referred to as *thixotropy*, manifests as a progressive increase in yield stress during resting periods and a concurrent degradation of the material structure under shear. To model thixotropic behaviour, Roussel's model is adopted [35], in which the static yield stress evolves according to:

$$\tau_0(t) = \tau_{0,i} + A_{\text{thix}}\, t, \tag{11}$$

where $\tau_{0,i}$ is the initial value of the yield stress, i.e., immediately after the shearing associated with extrusion and layer deposition, A_{thix} denotes the thixotropic build-up rate, and t represents the material resting time. A larger value of A_{thix} therefore corresponds to a faster structural rebuild of the material, leading to a more rapid recovery of mechanical strength after deposition.

3. Discrete model.

The equations of motion (1)–(2) are solved numerically using the Finite Element Method. Following a standard Galerkin formulation, the spaces on the domain Ω_t are defined as follows: the velocity trial space $S^u = \{\mathbf{u} \in H^1(\Omega_t) \mid \mathbf{u} = \bar{\mathbf{u}} \text{ on } \Gamma_D\}$ with corresponding test space $S_0^u = \{\mathbf{w} \in H^1(\Omega_t) \mid \mathbf{w} = \mathbf{0} \text{ on } \Gamma_D\}$, and the pressure trial and test space $S^p = L^2(\Omega_t)$, where $H^1(\Omega_t)$ and $L^2(\Omega_t)$ denote the standard Sobolev spaces [10]. The weak formulation is obtained by multiplying the momentum and mass balance equations by the test functions $\boldsymbol{w} \in S_0^u$ and $q \in S^p$ and integrating over Ω_t, leading to the problem of finding $\boldsymbol{u} \in S^u$ and $p \in S^p$ such that:

$$\int_{\Omega_t} \boldsymbol{w} \cdot \rho \frac{d\boldsymbol{u}}{dt} d\Omega_t = \int_{\Omega_t} \boldsymbol{w} \cdot (\nabla_{\boldsymbol{x}} \cdot (-p\boldsymbol{I} + \boldsymbol{\tau}) + \rho\boldsymbol{b}) \; d\Omega_t \quad \forall\, \boldsymbol{w} \in S_0^u, \tag{12}$$

$$\int_{\Omega_t} q\,(\nabla_{\boldsymbol{x}} \cdot \boldsymbol{u}) \; d\Omega_t = 0 \quad \forall\, q \in S^p. \tag{13}$$

The domain Ω_t is then discretized using first-order tetrahedra finite elements for both the velocity and pressure fields. However, this choice violates the Ladyzhenskaya–Babuška–Brezzi (LBB) condition [3] and therefore a proper stabilization must be introduced. In this work the Pressure-Stabilizing Petrov–Galerkin (PSPG) [14] formulation is adopted, which effectively introduces additional stabilizing terms in the weak form of the mass conservation:

$$\begin{aligned}&\int_{\Omega_t} q\left(\nabla_{\boldsymbol{x}}\cdot\boldsymbol{u}\right)\ d\Omega_t\\&-\sum_{e=1}^{n_e}\tau^e_{\text{PSPG}}\int_{\Omega_{e,t}}\frac{\nabla q_e}{\rho}\cdot\left(\nabla_{\boldsymbol{x}}\cdot\boldsymbol{\sigma}_e+\rho\boldsymbol{b}_e-\rho\frac{d\boldsymbol{u}_e}{dt}\right)d\Omega_{e,t}=0\quad\forall\ q\in S^p.\end{aligned}\tag{14}$$

Following [45] the stabilization parameter τ^e_{PSPG} can be computed for each element as:

$$\tau^e_{\text{PSPG}}=\left(\left(\frac{2}{\Delta t}\right)^2+\left(\frac{2\left\|\mathbf{u}_e\right\|_E}{h_e}\right)^2+9\left(\frac{4\mu^*_e}{\rho h_e^2}\right)^2\right)^{-\frac{1}{2}},\tag{15}$$

where: h_e is a characteristic local length scale, defined as the diameter of the sphere having the same volume as the tetrahedral element; $\|\mathbf{u}\|_E$ is a local velocity scale, computed as the Euclidean norm of the velocity at the element centroid; $\mu^*_e=\min(\mu_{\text{app},e},\mu_{\text{cut-off}})$ is a characteristic local viscosity, where $\mu_{\text{cut-off}}$ is a threshold cut-off introduced to prevent excessively large values and is hereafter set to $10^4\ Pa{\cdot}s$.

3.1. **Space discretization.**

The approximate solutions are sought in the discrete spaces $S^v_h\subset S^u$ and $S^p_h\subset S^p$, where the velocity and pressure fields are expressed in each finite element as interpolations of their respective nodal values:

$$u^i_e(\boldsymbol{x},t)=\sum_{a=1}^{n_e}N^u_a(\boldsymbol{x})U^i_{e,a}(t),\qquad p_e(\boldsymbol{x},t)=\sum_{a=1}^{n_e}N^p_a(\boldsymbol{x})P_{e,a}(t),\tag{16}$$

where n_e is the number of nodes in the element, $\boldsymbol{U}^i_e$ is the elementary vector of nodal velocities in the i-th direction, $\boldsymbol{P}_e$ is the elementary vector of the nodal pressures and N^u_a, N^p_a are the element shape functions for the velocity and the pressure respectively. The following semi-discretized in space equations are obtained:

$$\boldsymbol{M}_u\frac{d\boldsymbol{U}}{dt}+\boldsymbol{K}\boldsymbol{U}=\boldsymbol{F}_{ext}+\boldsymbol{D}^T\boldsymbol{P},\tag{17}$$

$$\boldsymbol{D}\boldsymbol{U}+\boldsymbol{L}\boldsymbol{P}+\boldsymbol{C}\frac{d\boldsymbol{U}}{dt}-\boldsymbol{H}=\boldsymbol{0},\tag{18}$$

where $\boldsymbol{M}_u$ is the velocity mass matrix, $\boldsymbol{K}$ is the deviatoric stiffness matrix, $\boldsymbol{F}_{ext}$ is the vector of the equivalent external forces, $\boldsymbol{D}$ is the discrete divergence operator matrix, $\boldsymbol{L}$ is the PSPG Laplacian matrix and $\boldsymbol{C}$ and $\boldsymbol{H}$ are respectively a global matrix and vector, associated to the PSPG terms providing consistency. A detailed description of these terms and their derivation can be found in [33].

3.2. **Time integration.**

Time discretization is performed by dividing the time history into constant steps Δt and approximating time derivatives with the backward Euler method. The resulting nonlinear equations are linearized and solved by means of Picard iterations. At each time step t_{n+1} for each iteration $k+1$, the updated velocities $\boldsymbol{U}^{k+1}_{n+1}$ and pressures $\boldsymbol{P}^{k+1}_{n+1}$ are computed solving the following strongly coupled linear system:

$$\begin{cases}\left(\frac{\boldsymbol{M}^k_{u,n+1}}{\Delta t}+\boldsymbol{K}^k_{n+1}\right)\boldsymbol{U}^{k+1}_{n+1}-\boldsymbol{D}^{T,k}_{n+1}\boldsymbol{P}^{k+1}_{n+1}=\boldsymbol{F}^k_{ext,n+1}-\frac{\boldsymbol{M}^k_{u,n+1}}{\Delta t}\boldsymbol{U}_n,\\\boldsymbol{L}^k_{n+1}\boldsymbol{P}^{k+1}_{n+1}+\left(\boldsymbol{D}^k_{n+1}+\frac{\boldsymbol{C}^k_{n+1}}{\Delta t}\right)\boldsymbol{U}^{k+1}_{n+1}=\frac{\boldsymbol{C}^k_{n+1}}{\Delta t}\boldsymbol{U}_n+\boldsymbol{H}^k_{n+1}.\end{cases}\tag{19}$$

Equations (19) are solved iteratively at each time step until convergence, measured in terms of the L^2 norms of the velocity and pressure errors, is reached.

3.3. **Particle finite element method.** The adoption of a Lagrangian framework over most of the computational domain offers several significant advantages. Notably, it enables natural tracking of free surfaces and eliminates the nonlinear convective term from the momentum equation. However, since nodal positions are updated in time based on their velocities, problems characterized by large deformations may result in severe mesh distortion. Without an appropriate corrective strategy, such mesh degradation can compromise numerical accuracy and stability, potentially rendering the simulation unfeasible.

A robust solution to this issue is provided by the Particle Finite Element Method (PFEM) [20, 8], which augments the updated Lagrangian formulation with an efficient remeshing algorithm. Originally conceived for the simulation of free-surface flows and wave-breaking phenomena [20], PFEM has since evolved into a versatile computational framework, successfully applied to a broad spectrum of materials and engineering problems. These include fluid–structure interaction [5, 17], multiphase and complex material flows [38, 32, 33], as well as industrial forming and manufacturing processes [19, 40].

More recently, PFEM has proven to be particularly well-suited for reproducing additive manufacturing scenarios, owing to its inherent capability to manage evolving interfaces, contact phenomena, and phase transitions within a unified formulation. For example, PFEM has been applied to reproduce extrusion and layer deposition processes in 3D printing with cementitious materials [26, 31, 34] or to model melt-pool dynamics in metal additive manufacturing [41, 12].

The fundamental idea of the PFEM is to employ a re-meshing strategy in which a new connectivity is generated whenever the existing finite elements result to be excessively distorted. The main steps of the re-meshing process are illustrated in Figure 1.

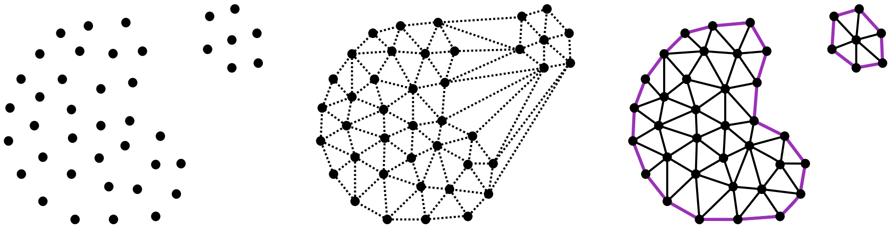
(A) (B) (C)

Figure 1. Re-meshing scheme in PFEM: initial point cloud (A); Delaunay triangulation convex hull (B); new-connectivity mesh, with free-surface identified by the α-shape method (C).

Throughout the analysis, mesh quality is continuously monitored and, whenever distortions become excessive, the mesh is deleted while preserving only the nodal positions, as illustrated in Figure 1-A. A new mesh connectivity is then generated using an efficient technique such as the Delaunay algorithm [43] (Figure 1-B). Finally, the α-shape method [11] is applied to identify the physical boundaries and determine the free surface (Figure 1-C). In practice, this procedure filters out highly distorted elements from the computational domain, as they are the most unlikely to belong to the fluid domain. For further details on the PFEM approach, the reader is referred to [20, 8].

PFEM provides a versatile and robust framework for modelling large deformations problems in fluid and solid mechanics. However, to fully exploit its potential in the context of extrusion-based additive manufacturing, the method must be complemented by a set of *ad hoc* computational techniques specifically devised to reproduce the 3D printing process. These techniques, introduced and discussed in detail in our previous works [31, 34, 28], are aimed at accurately representing the evolving computational domain, enforcing appropriate boundary conditions, and modelling contact interactions while minimizing spurious mass variations.

Within this framework, the extrusion is modelled using an Arbitrary Lagrangian–Eulerian (ALE) formulation [10], which enables the reproduction of nozzle translations and rotations while simultaneously imposing boundary conditions at the nozzle outlet to ensure a continuous material flow. Contact with the rigid print bed is enforced through kinematic constraints on nodal positions, reducing artificial volume variations due to remeshing [13]. In addition, a dedicated interlayer contact and merging strategy is adopted to promote smooth and consistent bonding between successive layers.

4. **3D printing numerical framework for complex objects.**

Despite the robustness of the framework, PFEM - as well as other computational fluid dynamics techniques - has so far only been applied to model extrusion and layer deposition in standard scenarios. Most of the studies in the literature focus on simulating few superimposed rectilinear layers, mainly due to computational constraints [30]. In contrast, the objective of the present work is to demonstrate how increasingly complex and extended printing processes can now be simulated, paving the way for the numerical analysis of full-scale, realistic prints.

Apart from an efficient and optimized FEM solver, achieving this goal requires a robust strategy to import and reproduce printer instructions within the numerical model. In extrusion-based additive manufacturing, such instructions are typically provided in the form of G-code, a machine-level language that encodes the printing toolpath as a sequence of commands specifying nozzle positions, velocities, extrusion rates, and auxiliary operations. The toolpath, defined as the spatial trajectory followed by the nozzle during material deposition, plays a central role in determining both the geometry and the quality of the printed object [16]. In the following section, we describe in detail the automatic procedure adopted to parse G-code files and translate the corresponding toolpath into suitable time-dependent boundary conditions governing nozzle motion within the PFEM framework.

4.1. **Nozzle motion reconstruction from G-code.**

In 3D printing, the ideal continuous toolpath generated by the design software is typically converted by the slicer into G-code, which represents the path as a polyline composed of piecewise-linear segments. Each segment i is defined by its end-point coordinates in space and an associated feed rate, which can be interpreted as the magnitude of the nozzle translational velocity along that segment, $v_{p,i}$.

Therefore, in the numerical simulation, the imposed nozzle trajectory can be reconstructed from the G-code by extracting the ordered list of target positions associated with consecutive deposition commands, yielding the set of points $\{\mathbf{x}_k\}_{k=1}^{N}$, where N denotes the total number of points along the path. Each consecutive pair of points defines a straight toolpath segment. At any simulation time t, the virtual nozzle moves along a single active segment indexed by $i \in \{1, \dots, N-1\}$. The segment length can be computed as:

$$\ell_i = \|\mathbf{x}_{i+1} - \mathbf{x}_i\|\,, \tag{20}$$

and the piecewise constant printing speed $v_{p,i}$, derived from the feed rate, is imposed along the segment direction, giving the nozzle velocity:

$$\mathbf{v}(t) = v_{p,i} \frac{\mathbf{x}_{i+1} - \mathbf{x}_i}{\ell_i}. \tag{21}$$

Moreover, the traversal time of segment i can be computed as

$$\Delta t_i = \frac{\ell_i}{v_{p,i}}, \tag{22}$$

and the cumulative traversal time up to the end of segment i is

$$T_i = \sum_{k=1}^{i} \Delta t_k. \tag{23}$$

The active segment index is advanced when the simulation time satisfies $t \geq T_i$. Repeating this procedure until $i = N - 1$ provides a piecewise-linear, constant-speed representation of the nozzle motion, which can be directly used to impose kinematic boundary conditions in the finite element simulation.

4.2. **Admissible time step.** Let $\Delta s \simeq l_i$ denote the spatial resolution of the toolpath, defined as the average distance between consecutive polyline points, Δt be the simulation time step and v_p the prescribed nozzle speed, assumed hereafter for simplicity as constant along the whole toolpath. During a single time step, the nozzle travels a characteristic distance $\Delta h = v_p \Delta t$. If Δh exceeds Δs, clearly the motion along the toolpath cannot be accurately resolved, potentially producing spurious trajectories. Therefore, a necessary condition to correctly capture the toolpath is given by:

$$\Delta h = v_p\, \Delta t \leq \Delta s. \tag{24}$$

The importance of this condition is illustrated in Figure 2. The toolpath is discretized with a characteristic spacing $\Delta s = 0.00148$ m. For a constant printing speed $v_p = 0.1$ m/s, three different simulation time steps are considered: $\Delta t = 0.01$, 0.015, and 0.02 s, corresponding to nozzle travel distances inside a time step of $\Delta h = 0.001$, 0.0015, and 0.002 m, respectively. The larger time steps are associated to $\Delta h = 0.0015$ and 0.002 m both exceeding Δs and thus the nozzle motion skips intermediate discretization points, resulting in under-sampling of the polyline and an incorrect reconstruction of the intended toolpath. In contrast, the smaller time step yields $\Delta h = 0.001$ m $< \Delta s$ ensuring adequate spatial sampling of the toolpath.

4.3. **Admissible toolpath discretization.** Reducing the time step often allows the toolpath to be properly resolved; however, this requires solving the Navier–Stokes equations more frequently, which can significantly reduce computational efficiency. An alternative approach would be to adjust the toolpath resolution to ensure that the motion can be reproduced by large enough time steps. Referring to the previously adopted time steps, Figures 3 illustrate two toolpath samplings with adjusted Δs, which now allow to accurately resolve the motion even for $\Delta t = 0.015$ s.

Although the motion is correctly resolved, Figure 3-A corresponds to an excessively coarse toolpath discretization (Δs), leading to a poor representation of its

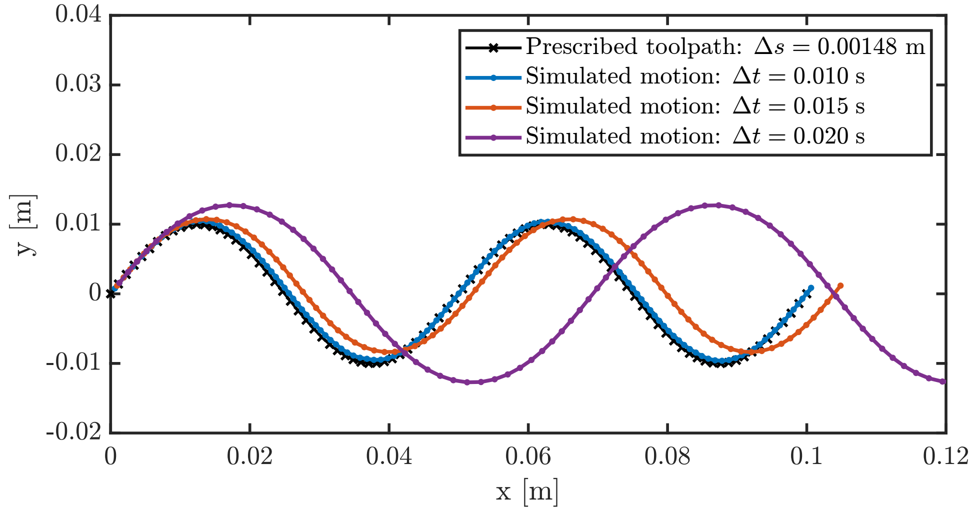

FIGURE 2. Influence of the simulation time step on the nozzle motion reproduction, for a fixed toolpath discretization $\Delta s = 0.00148$ m and printing velocity magnitude of $v_p = 0.1$ m/s.

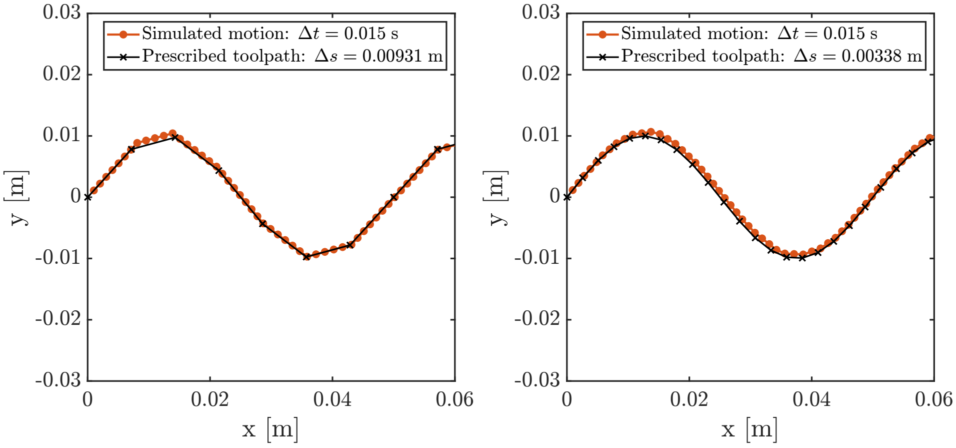

(A)

(B)

FIGURE 3. Two toolpath discretizations that ensure accurate motion resolution for a fixed simulation time step of $\Delta t = 0.015,$s and a printing velocity magnitude of $v_p = 0.1$ m/s.

geometric features. Figure 3-B provides instead a good compromise between accuracy and efficiency, reproducing the toolpath with enough fidelity while maintaining $\Delta s > \Delta h$ for a time step of $\Delta t = 0.015$ s. This time step is sufficiently large for practical computations of extrusion and layer deposition; in fact, even larger time steps - although potentially allowed by the toolpath - may not be admissible due to other requirements, such as the correct reproduction of the inflow or the accurate resolution of inter-layer contact.

4.4. **Arc-length resampling.** Toolpaths generated by slicers, custom Grasshopper-Rhino scripts, or other robotic planning tools are often incompatible with the requirements of transient FEM simulations. Their discretization can be highly non-uniform or unnecessarily dense, imposing impractically small time-step constraints. To address this limitation, we propose an automatic toolpath resampling strategy that enforces approximately uniform point spacing. This approach preserves accurate nozzle motion while allowing the use of the largest stable time step permitted by the simulation.

To this end, we adopt an arc-length–based resampling strategy. The approach is inspired by the methodology introduced in [15] for iteratively transforming a closed piecewise-linear polyline into an equilateral polygonal curve. Unlike their method, which preserves the number of points and adapts edge lengths through multiple iterations - potentially producing an equilateral curve that deviates significantly from the original polyline - our objective is simply to introduce a new set of points that remain as close as possible to the original polyline while being uniformly spaced.

Accordingly, we apply only a single iteration of the algorithm, corresponding to a single arc-length resampling of the polyline with a user-prescribed inter-point spacing. This yields a curve that remains close to the original while providing a quasi-uniform distribution of vertices consistent with the specified spacing.

Starting from the original polyline $\{\mathbf{x}_k\}_{k=1}^{N}$, we first compute the cumulative arc length along the toolpath:

$$s_1 = 0, \quad s_k = \sum_{j=1}^{k-1} \|\mathbf{x}_{j+1} - \mathbf{x}_j\|, \quad k = 2, \dots, N, \tag{25}$$

where $\|\cdot\|$ denotes the Euclidean distance in 3D, and the total arc length is $S = s_N$. Next, we generate the resampled points $\{\tilde{\mathbf{x}}_m\}_{m=0}^{M}$ by uniformly sampling along the cumulative arc length of the original polyline:

$$\tilde{s}_m = m\,\Delta s, \quad m = 0, 1, \dots, M, \text{ with } M = \left\lfloor \frac{S}{\Delta s} \right\rfloor, \tag{26}$$

where Δs is the target spacing, chosen to satisfy the time-step resolution constraint (24).

Specifically, for each resampled point, we first identify the original polyline segment $[\mathbf{x}_k, \mathbf{x}_{k+1}]$ that contains its cumulative arc length $\tilde{s}_m \in [s_k, s_{k+1}]$, and then compute its coordinates via linear interpolation:

$$\tilde{\mathbf{x}}_m = \mathbf{x}_k + \frac{\tilde{s}_m - s_k}{s_{k+1} - s_k}(\mathbf{x}_{k+1} - \mathbf{x}_k). \tag{27}$$

4.5. **Time step cutting.** In Figure 3-B it can be observed that, even when $\Delta h < \Delta s$, a small but systematic error is introduced in the toolpath. This error increases proportionally with the time-step size Δt. This phenomenon, commonly referred to as the *overshooting problem*, occurs when the distance travelled by the nozzle during a single time step is not an exact multiple of the spatial discretization of the toolpath. As a result, there may be instances in which the distance travelled within one time step exceeds the remaining distance to the next discretization point. In such cases, the nozzle position is updated beyond the target point, leading to a cumulative spatial error along the toolpath, as shown in Figure 4.

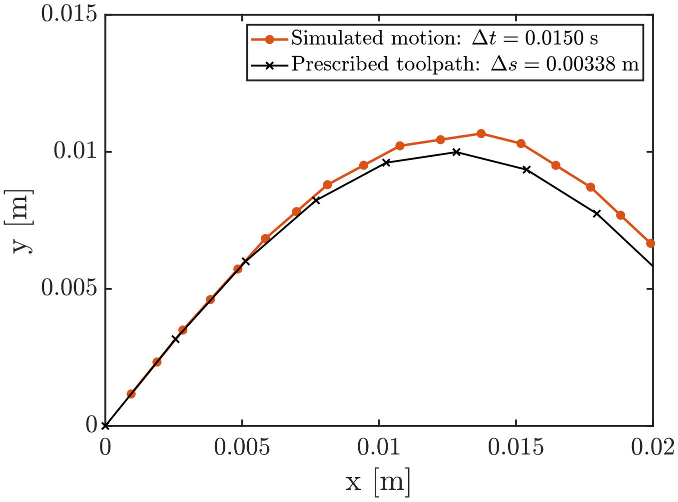

FIGURE 4. Close-up view of the overshooting problem.

This issue can be efficiently mitigated by temporarily reducing the time step when an overshoot of a discretization point would occur and keeping the base time step constant for the remainder of the simulation. Let $\mathbf{x}_k$ denote the next toolpath point to be reached and $\mathbf{x}(t)$ the current nozzle position. If the distance travelled by the nozzle in a time step Δt is larger than the distance between the next toolpath point and the current nozzle position:

$$v_p \Delta t > d_k = \|\mathbf{x}_k - \mathbf{x}(t)\|, \tag{28}$$

then, the nozzle would overshoot the target point. To prevent this, the current time step is reduced to:

$$\Delta t_{\text{cut}} = \frac{d_k}{v_p}, \tag{29}$$

so that the nozzle reaches $\mathbf{x}_k$ exactly. Once the point is reached, the simulation resumes using the original base time step Δt.

This temporarily time-step reduction ensures that each toolpath point is reached accurately, thereby eliminating cumulative spatial errors without requiring a globally smaller time step and thus preserving computational efficiency. Moreover, this approach improves the robustness of the overall procedure, as it allows the algorithm to better accommodate deviations from the target toolpath spacing that may arise from the arc-length resampling procedure, particularly in the vicinity of sharp corners.

5. **Results.** This section is divided into two parts. The first part presents a dedicated validation of the proposed numerical framework for 3D printing simulation. Although its predictive capabilities were previously demonstrated for different printing parameters in [31] and for different material properties in [34], the present implementation introduces substantial modifications to the solution strategy. In particular, the finite element solver adopted here employs an implicit time discretization scheme, resulting in a stabilized, fully monolithic system. This approach ensures stable solutions for significantly larger time steps than those achievable with the

explicit solvers adopted in [31, 34], thereby enabling larger-scale simulations and the assessment not only of extrudability, but also of buildability.

The second part focuses on the numerical simulation of 3D printing processes involving complex, hollow, parametric geometries, including overhangs and intricate shapes, in order to demonstrate the capability of the framework to accurately address more advanced and realistic applications.

5.1. **Validation: three layers wall.** To validate the numerical model, the printing of three superimposed rectilinear layers, each 300 mm in length, is reproduced. The material and printing parameters are taken from [44]. Specifically, a cementitious mortar characterized by density $\rho = 2100$ kg/m^3, yield stress $\tau_0 = 630$ Pa and plastic viscosity $\mu = 7.5$ Pa $\cdot$ s is considered. The printing parameters are: nozzle diameter $\phi_\mathrm{n} = 25\,\mathrm{mm}$, nozzle height $h_\mathrm{n} = 12.5\,\mathrm{mm}$, printing velocity $v_\mathrm{p} = 30\,\mathrm{mm/s}$, and flow velocity $u_\mathrm{f} = 33.6\,\mathrm{mm/s}$. At the end of each layer, the nozzle is raised by $\Delta z = 12.5\,\mathrm{mm}$ without interrupting the printing process, thereby generating a single continuous filament wall.

Figure 5 compares the extracted numerical cross-sections with the experimental results reported in [44]. A very good agreement is observed in all cases, with the numerical profiles closely overlapping the experimental ones, both for the single-layer configuration and for the multi-layer case. This confirms the accuracy of the model in reproducing deposition on a rigid substrate as well as interlayer contact.

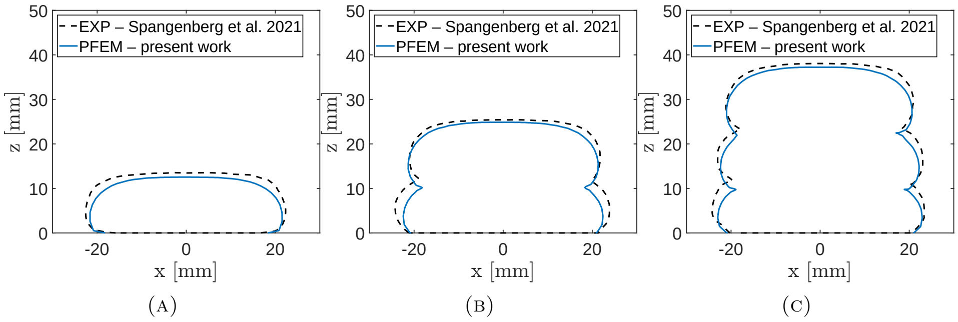

(A) (B) (C)

FIGURE 5. Comparison of the cross-sections obtained from the print of one (A), two (B) and three (C) layers for the present work with the experimental data (EXP) from [44].

5.2. **Complex parametric objects.** This section addresses the simulation of complex, parametric, multi-layer objects. Three case studies are considered, conceived either as column segments or as generic structural components. These examples are representative of the intricate geometries typically encountered in the practical 3D printing of structural or decorative elements using clay or cementitious materials. The procedures used to generate their geometries and the corresponding toolpaths by means of external software are described in detail in the following. Successively, when imported in the simulation environment as G-codes the toolpaths are automatically treated using the techniques introduced earlier, before starting numerical simulations. The numerical analyses have the objective of assessing printing stability and of predicting the geometric conformity of the final printed objects.

5.2.1. *Geometry design and toolpath planning.* The three-dimensional geometry of the three objects, as well as the rationale underlying their conceptualization, are detailed below with reference to Figure 6.

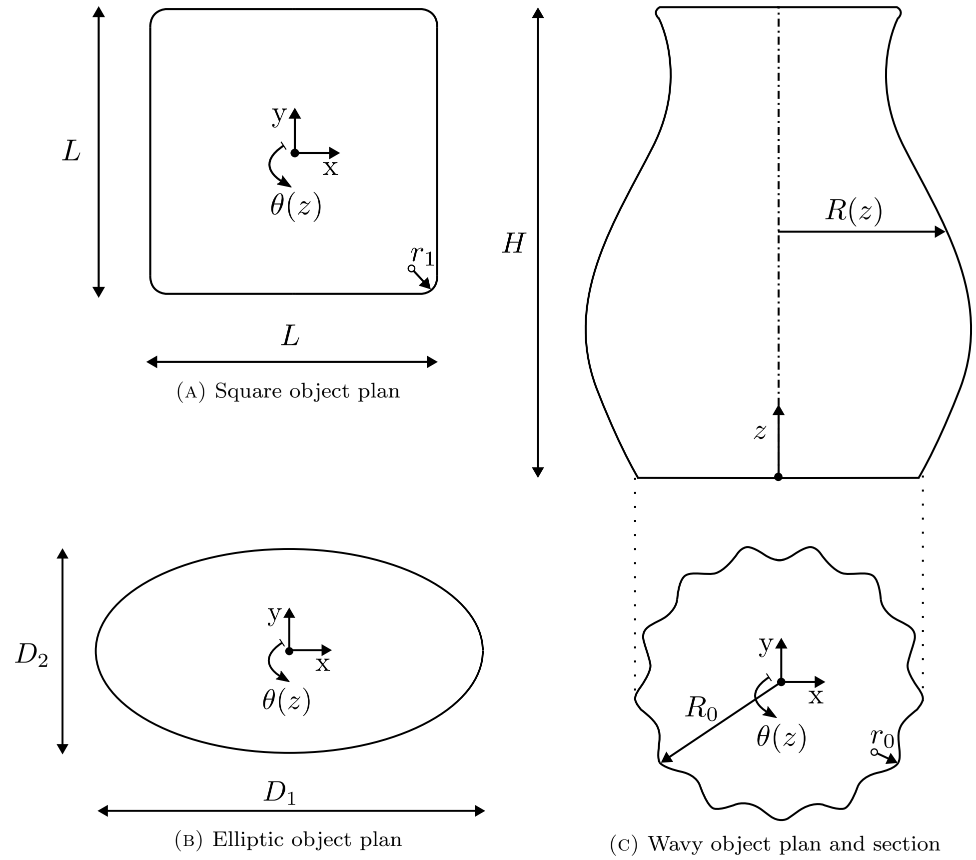

(A) Square object plan

(B) Elliptic object plan

(C) Wavy object plan and section

FIGURE 6. Geometrical parameters regulating the shape of the three objects.

1. *Square object.* The first object features a square planar base with side length $L = 100\,\text{mm}$ and rounded corners defined by curvilinear arcs of radius $r_1 = 6\,\text{mm}$, as shown in Figure 6-A. The planar base is used to generate the three-dimensional geometry by means of vertical translations and in-plane rotations. Particularly, the rotation angle varies linearly with the height according to:

$$\theta(z) = \psi_1 z, \quad \text{with } \psi_1 = 1^\circ/\text{mm}.$$

2. *Elliptic object.* The second object presents an elliptical planar base, illustrated in Figure 6-B, characterized by a major axis $D_1 = 120\,\text{mm}$ and a minor axis $D_2 = 60\,\text{mm}$. The base is translated vertically while being simultaneously rotated according to

$$\theta(z) = \psi_2 z, \quad \text{with } \psi_2 = 1^\circ/\text{mm}.$$

3. *Wavy object.* The third object features a more complex planar base, initially defined as a circle of radius $R_0 = 43\,\text{mm}$, perturbed by small periodic undulations of amplitude $r_0 = 3\,\text{mm}$, as shown in Figure 6-C. During vertical translation, the base undergoes an in-plane expansion and contraction:
$$R(z) \simeq R_0 \left[0.22 \sin\left(\frac{z}{1.88 R_0} \right) + 1 \right],$$
which modulates the overall shape of the object. Simultaneously, the base is also rotated according to:
$$\theta(z) = \psi_3 z, \quad \text{with } \psi_3 = 0.64^\circ/\text{mm}.$$

The three objects are constructed to the total height of $H = 140\,\text{mm}$. The vertical offset between successive layers is set to $\Delta z = 7\,\text{mm}$, resulting in a total of 20 layers. In practice, the CAD geometries are developed in Rhino 3D using Grasshopper, leveraging the platform's strengths in parametric design. These software also facilitate slicing and toolpath generation, which are subsequently provided to the numerical model in the form of G-code. Figures 7-A, B, C show the final CAD geometries obtained for the three objects, assuming idealized circular filament layers with a diameter equal to the vertical offset Δz. The corresponding sliced toolpaths are illustrated in Figures 7-D, E, F.

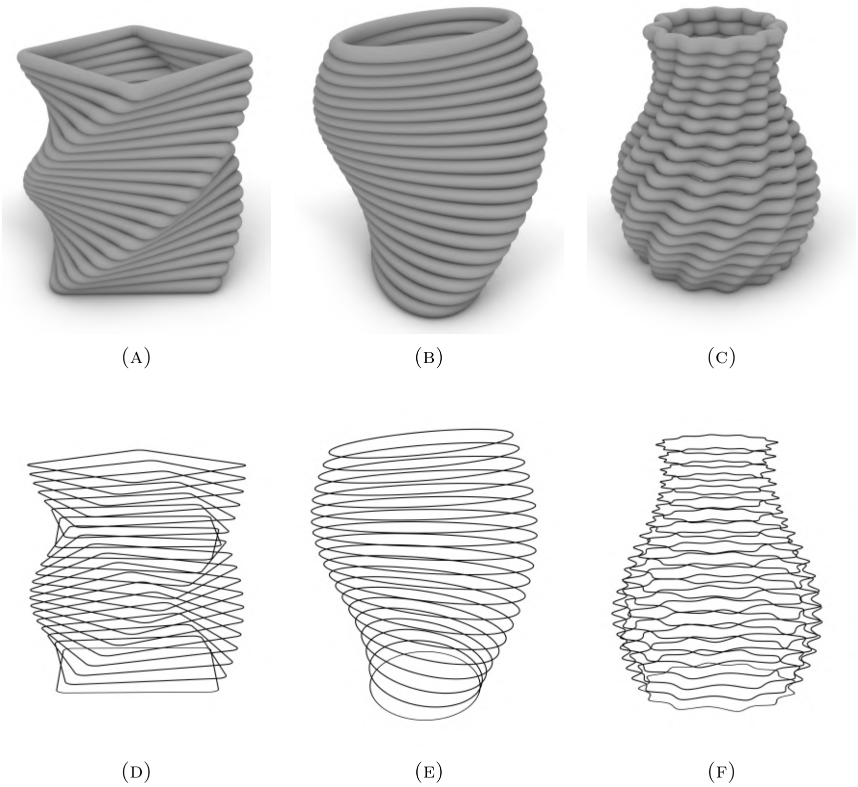
(A) (B) (C)

(D) (E) (F)

Figure 7. Three-dimensional CAD geometries (A–C) and corresponding sliced toolpaths (D–F).

5.2.2. *Process parameters and material properties.* The nozzle is assumed to be circular, with a diameter of $\phi_n = 10\,\text{mm}$. Its initial distance from the rigid plane is set to $h_n = 7\,\text{mm}$, and it is subsequently raised by a vertical increment of $\Delta z = 7\,\text{mm}$ after the deposition of each layer. The printing parameters are preliminary calibrated through single-layer simulations to obtain a target layer height of approximately $h \simeq 7\,\text{mm}$. This is realized by setting the printing velocity to $v_p = 60.4\,\text{mm/s}$ and the flow velocity to $u_f = 80\,\text{mm/s}$. Overall, a layer-pressing printing strategy is achieved.

The material properties correspond to those of a generic yield-stress fluid obeying the Bingham constitutive law, representative for example of cementitious materials. The density is set to $\rho = 2200\,\text{kg/m}^3$ and the plastic viscosity to $\mu = 10\,\text{Pa}\cdot\text{s}$; both quantities are kept constant throughout the study. In contrast, different values of the initial yield stress, namely $\tau_{0,i} = 1500, 3000, 6000,$ and $12000\,\text{Pa}$, are investigated, together with different values of the thixotropic parameter $A_{\text{thix}} = 10, 15, 20,$ and $40\,\text{Pa/s}$, as showcased in Table 1. The selected materials span a progression from low buildability (M1) to highly buildable systems (M4), reflecting typical rheological behaviour of cement-based materials, where yield stress and structural build-up rate are generally correlated due to particle flocculation and early hydration [36]. This setup therefore enables a systematic analysis of the joint influence of static yield stress and its time-dependent evolution on printing stability and geometric conformity.

Table 1. Definition of material sets used in the simulations.

Material	ρ [kg/m^3]	μ [Pa·s]	$\tau_{0,i}$ [Pa]	A_{thix} [Pa/s]
M1	2200	10	1500	10
M2	2200	10	3000	15
M3	2200	10	6000	20
M4	2200	10	12000	40

5.2.3. *Virtual printing simulations.* Regarding the numerical setup, all simulations employed a quasi-uniform mesh size of characteristic length $h \simeq 1.57\,\text{mm}$, resulting in approximately 2×10^5 nodes and about 1×10^6 elements by the end of the printing process. Despite being executed in parallel, the simulations slowed significantly toward the final stages due to the growing computational domain. This is expected, since the number of degrees of freedom increases progressively with the continuous inflow of new material and the cost of the direct solver scales superlinearly with system size [24]. Consequently, individual simulations required up to several days to complete.

For each geometry - square, elliptic, and wavy - four simulations were performed to reproduce the virtual printing process under different combinations of material properties. The total printing time depends on the geometry and it is equal to 129.04 s for the square object, 96.24 s for the elliptic object, and 94.28 s for the wavy object.

A constant time step of $\Delta t = 0.01\,\text{s}$ was adopted in all simulations. Accordingly, the G-code generated by the custom Grasshopper slicer was resampled with the approach proposed in Section 4.4 to ensure a spatial resolution of the nozzle motion compatible with the kinematic constraint in (24). At each time step, the nozzle position is updated based on the prescribed velocity vector (21), ensuring consistent toolpath tracking, while the inflow boundary conditions are enforced within the ALE framework [31]. The time-step cutting procedure of Section 4.5 was also automatically applied during the simulations to prevent overshooting of toolpath points while maintaining computational efficiency.

Initially we report and comment results for material M4, for which the best performances were observed. Figures 8, 9, and 10 illustrate snapshots from the virtual printing process of the three objects with this material. During the initial stages of printing (panels A–C), a common behaviour is observed regardless of the objects geometry: the dominant, and practically the only significant, source of stress arises from the extrusion and layer deposition processes. Owing to the layer-pressing strategy, the flow of material from the nozzle generates high pressure concentrations and plastic deformations in the surrounding material, leading to yielding of the substrate layer and localized stress concentrations in its vicinity. Due to their highly localized nature, these stresses have a limited impact on the overall structural stability at this stage, although they contribute to shaping the layer geometry. As the number of deposited layers increases (panels D–F), geometry-dependent stress patterns begin to emerge, which need to be analysed separately.

In particular, for the square-base object Figures 8-D, E, F show that significant stresses progressively develop along four helical bands wrapping around the object, located approximately at the midspan of each side. Despite the high yield stress of the material, both the stresses and the associated deformations increase and become especially pronounced during the deposition of the final layers. This suggests that the object may approach an unstable state if additional layers were to be printed.

For the elliptic geometry, as printing progresses, stresses tend to concentrate in regions where the geometry exhibits marked changes in concavity, generally below overhangs, as shown in Figures 9-D, E, F. Although these stresses, combined with those induced by the extrusion process, induce some non-negligible deformations, the structure remains stable throughout the printing process and it is able to preserve the overall shape, owing to the high yield stress of the material.

Finally, in the case of the wavy object, stresses progressively concentrate along multiple narrow helical bands wrapping around the object, particularly near the re-entrant regions of the undulations (Figures 10-D, E, F). These stresses result in increasingly pronounced deformations as printing progresses, nevertheless, this structure appears overall more stable than the previously analysed objects. This is likely because the undulated deposition of the layers enhances the stiffness of the walls, jointly with the fact that the object has a tapered shape which narrows with increasing height.

Figure 11 shows the final shapes of the three objects obtained under the best printing material M4, along with the static yield stress distribution in the material at rest. As can be seen, the numerical model is able to continuously capture the evolution of the mechanical properties in the deposited layers, providing a process-dependent and realistic representation of the mechanical response of the printed objects.

5.2.4. *Buildability and geometrical conformity predictions.* A preliminary simulation was carried out to evaluate the exact geometrical shape of the extruded filament using the printing and material parameters specified above. It is worth noting that, for the extrusion of a single layer on a rigid substrate, using either the lowest ($\tau_0 = 1500$ Pa) or the highest ($\tau_0 = 12000$ Pa) yield stress values considered

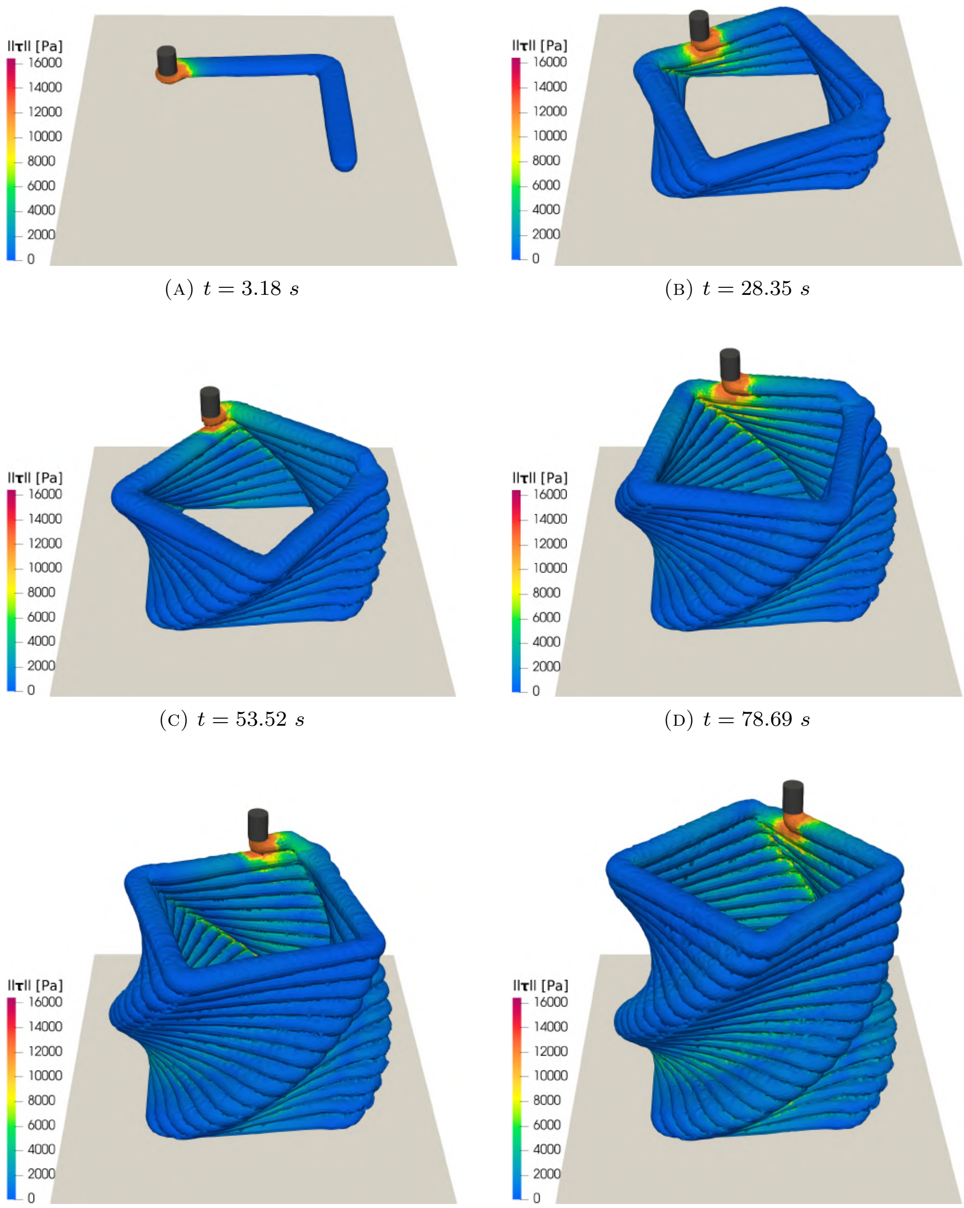

(A) $t = 3.18\ s$ (B) $t = 28.35\ s$

(C) $t = 53.52\ s$ (D) $t = 78.69\ s$

(E) $t = 103.87\ s$ (F) $t = 128.80\ s$

FIGURE 8. Virtual printing process of the square object, showing the von Mises stress distribution.

in this study has a negligible effect on the final layer shape. Both values exceed the minimum yield stress required for the material to maintain its shape under gravity-induced stresses [34]. Consequently, also the time-dependent evolution of the yield stress can be safely neglected in the single-layer simulation. In contrast, for the multi-layer 3D printing simulations, the combined effect of static yield stress

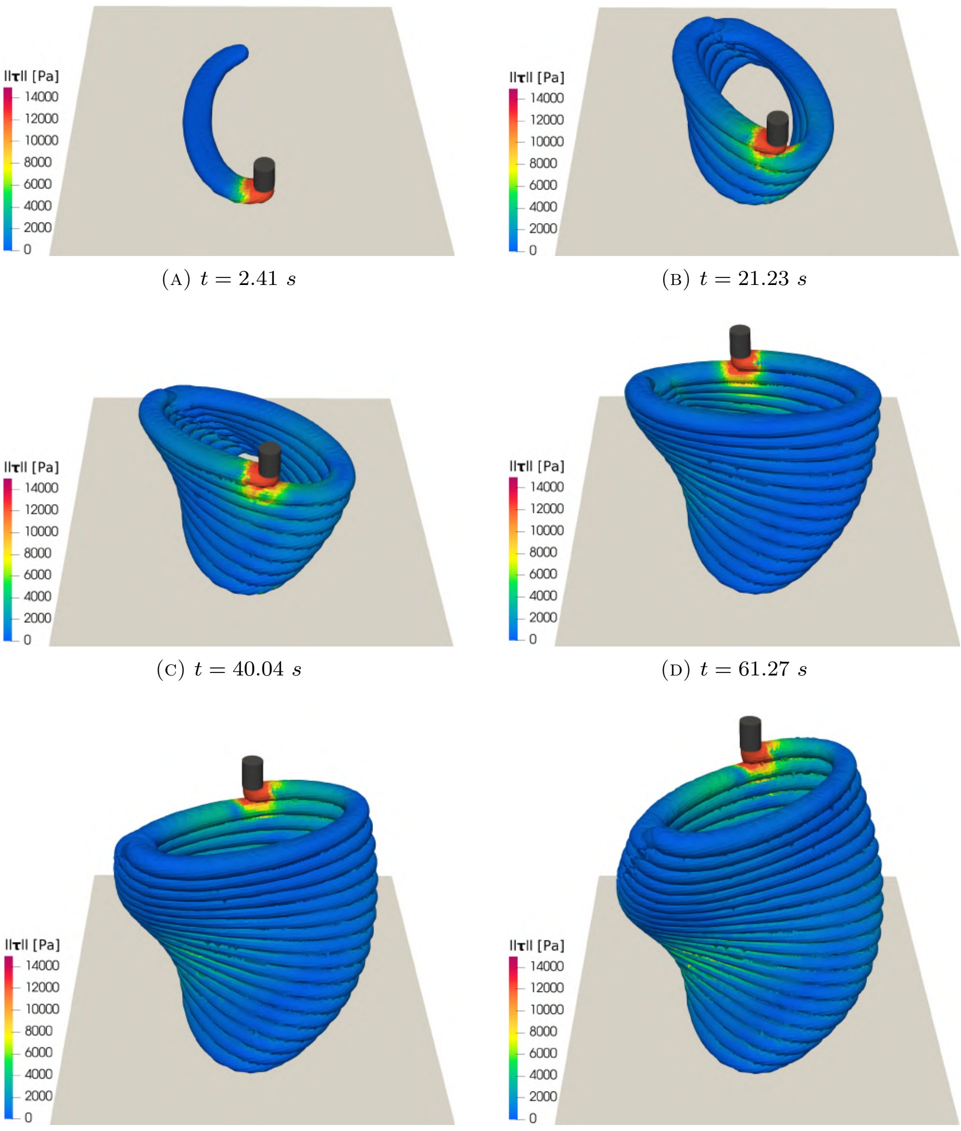

(A) $t = 2.41\ s$ (B) $t = 21.23\ s$

(C) $t = 40.04\ s$ (D) $t = 61.27\ s$

(E) $t = 80.08\ s$ (F) $t = 94.31\ s$

FIGURE 9. Virtual printing process of the elliptic object, showing the von Mises stress distribution.

and thixotropic behaviour becomes critical and it is expected to strongly influence buildability.

Results provided the full 3D geometrical shape of the first layer, from which it was possible to extract general information such as layer width $w \simeq 15\ mm$ and layer height $h \simeq 7\ mm$, as well as the full outline of the cross-sectional profile. The latter can be utilized to construct what we will refer to as the *reference geometry* of the three objects. The reference geometry represents the 3D shape that the object would have if the material, immediately after deposition, experienced no further

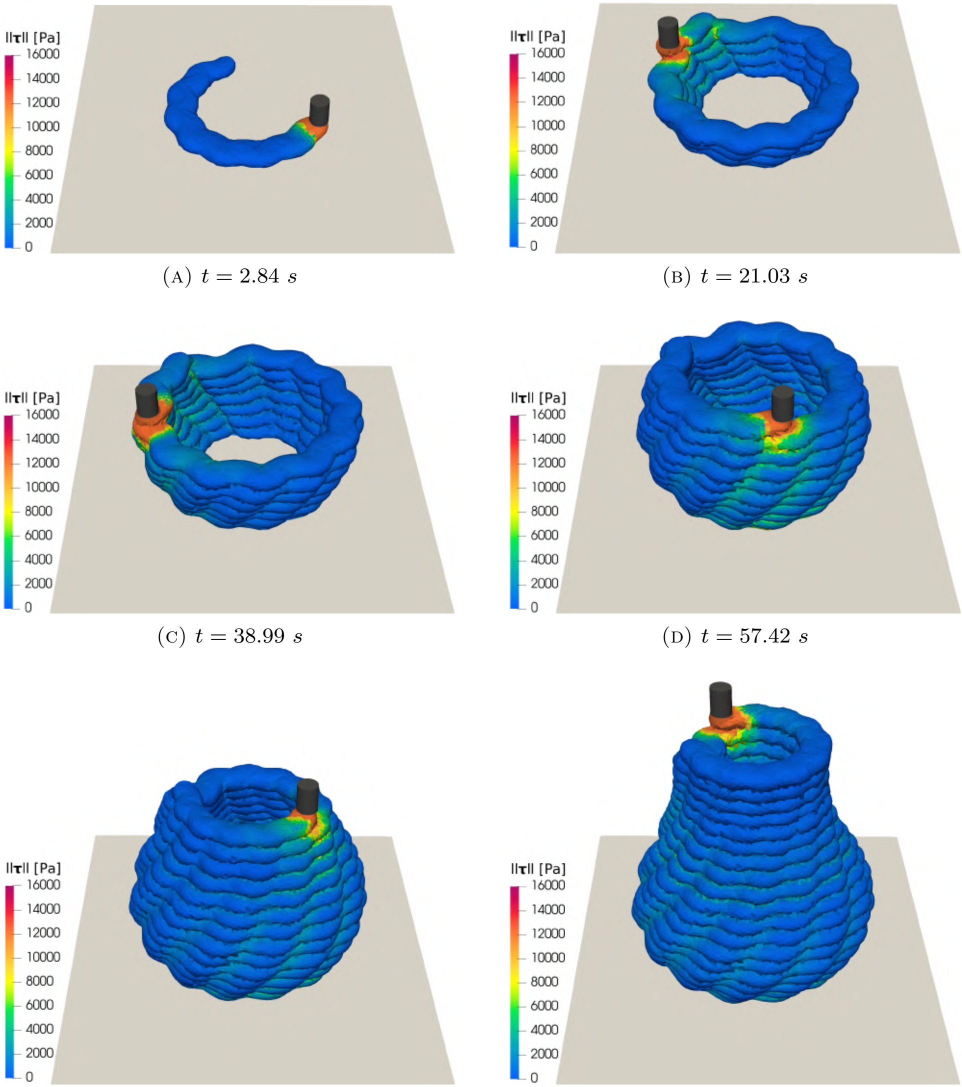

(A) $t = 2.84\ s$

(B) $t = 21.03\ s$

(C) $t = 38.99\ s$

(D) $t = 57.42\ s$

(E) $t = 75.61\ s$

(F) $t = 93.81\ s$

FIGURE 10. Virtual printing process of the wavy object.

deformation under the weight of subsequent layers. Practically, this undeformed geometry corresponds to a situation in which all layers have the same cross-section. While this scenario is not achievable in practice, it serves as a valuable benchmark for comparing deviations of the virtually printed geometries with respect to the targeted shapes. This allows for the evaluation of the effects of material properties on the overall deformation and stability of the printed object.

To create the reference geometry in Rhino 3D + Grasshopper, the filament cross-sectional outline from the preliminary analysis is imported as a closed curve, translated to align its centroid with the toolpath's start, and by means of a *sweep operation*, extruded along the toolpath itself (Figure 12-A, B). The reference geometries obtained for the three objects are represented in Figure 12-C, D, E also

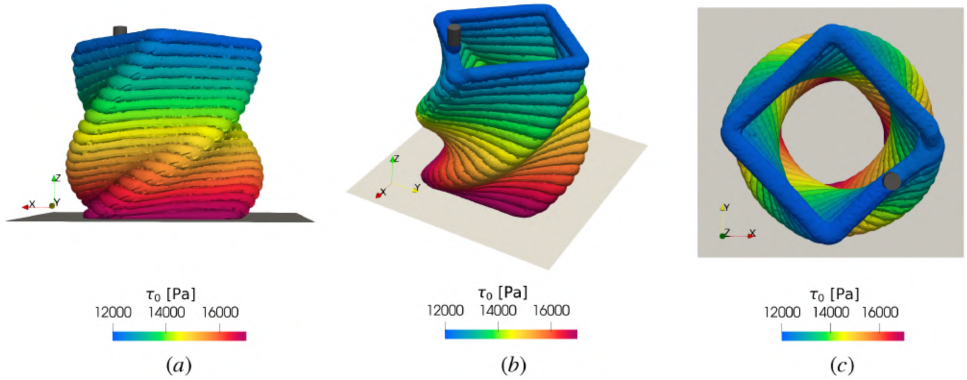

(A) Square object

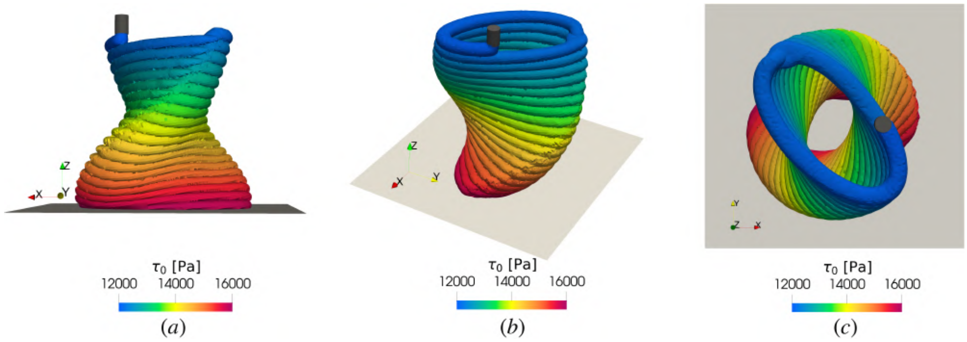

(B) Elliptic object

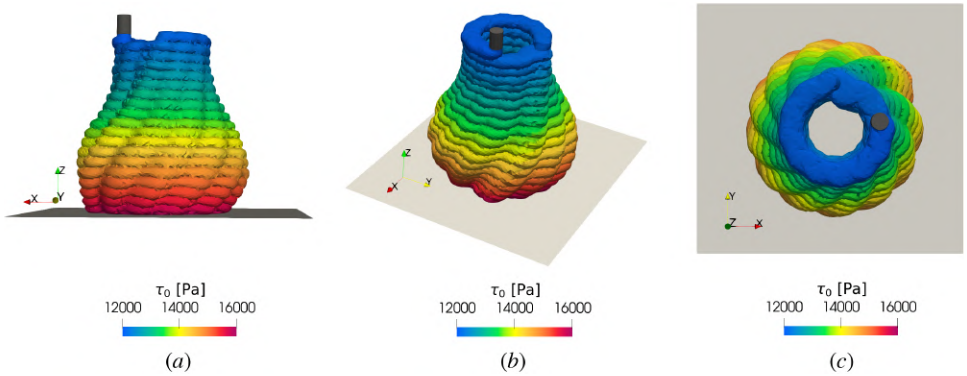

(C) Wavy object

FIGURE 11. Static yield stress distribution at the end of the printing process in the square, elliptic, and wavy objects.

indicating the position in which the section, to be used for the comparison with the virtually printed objects, is extracted.

Figures 13 present a quantitative comparison between the reference cross-sections and those obtained from the virtual printing processes for the square, elliptic, and

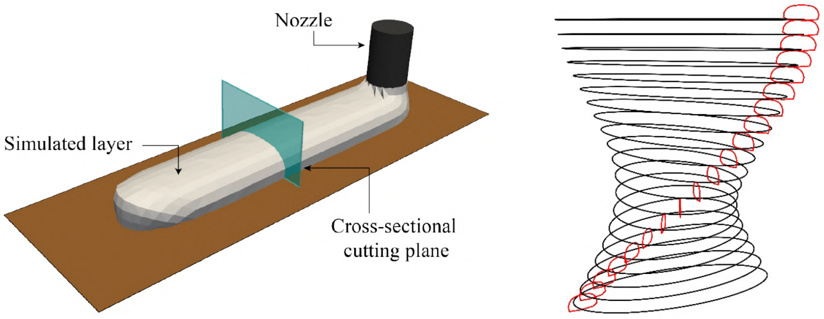

(A) Single layer PFEM simulation

(B) Sweep operation

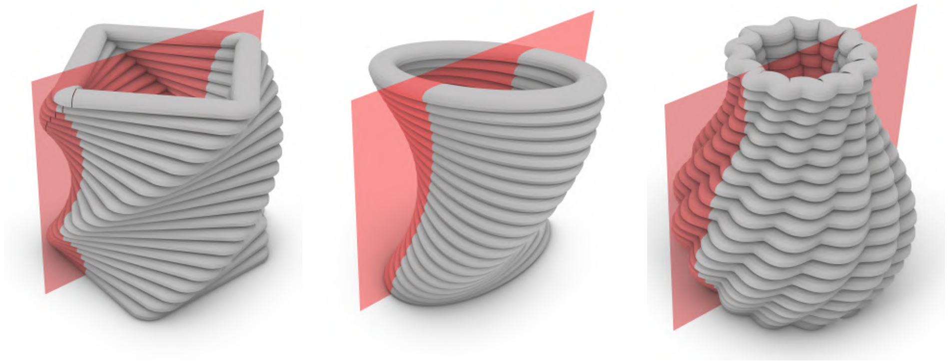

(C) Square object

(D) Elliptic object

(E) Wavy object

FIGURE 12. Construction of the reference geometry for the elliptic object (A, B). Subsequent extraction of the mid cross-sections for the three resulting reference geometries (D–F).

wavy objects, respectively, using the different combinations of material parameters defined earlier. Across all geometries, material performance plays a decisive role in the stability of the printed objects. Low initial static yield stress and slow thixotropic build-up result in pronounced early-stage deformations, whereas increasing both parameters progressively enhances structural integrity and geometric fidelity.

For the lowest-performance material (M1), all objects experience rapid loss of stability. The square object (Figure 13-A) collapses around the 14th layer. The elliptic object (Figure 13-B) even sooner, losing stability and collapsing inward at the 10th. The wavy object (Figure 13-C) tolerates deformation for a longer time but still undergoes severe base folding and loss of shape by the 18th layer. Overall, this material is clearly inadequate for 3D printing regardless the considered geometry.

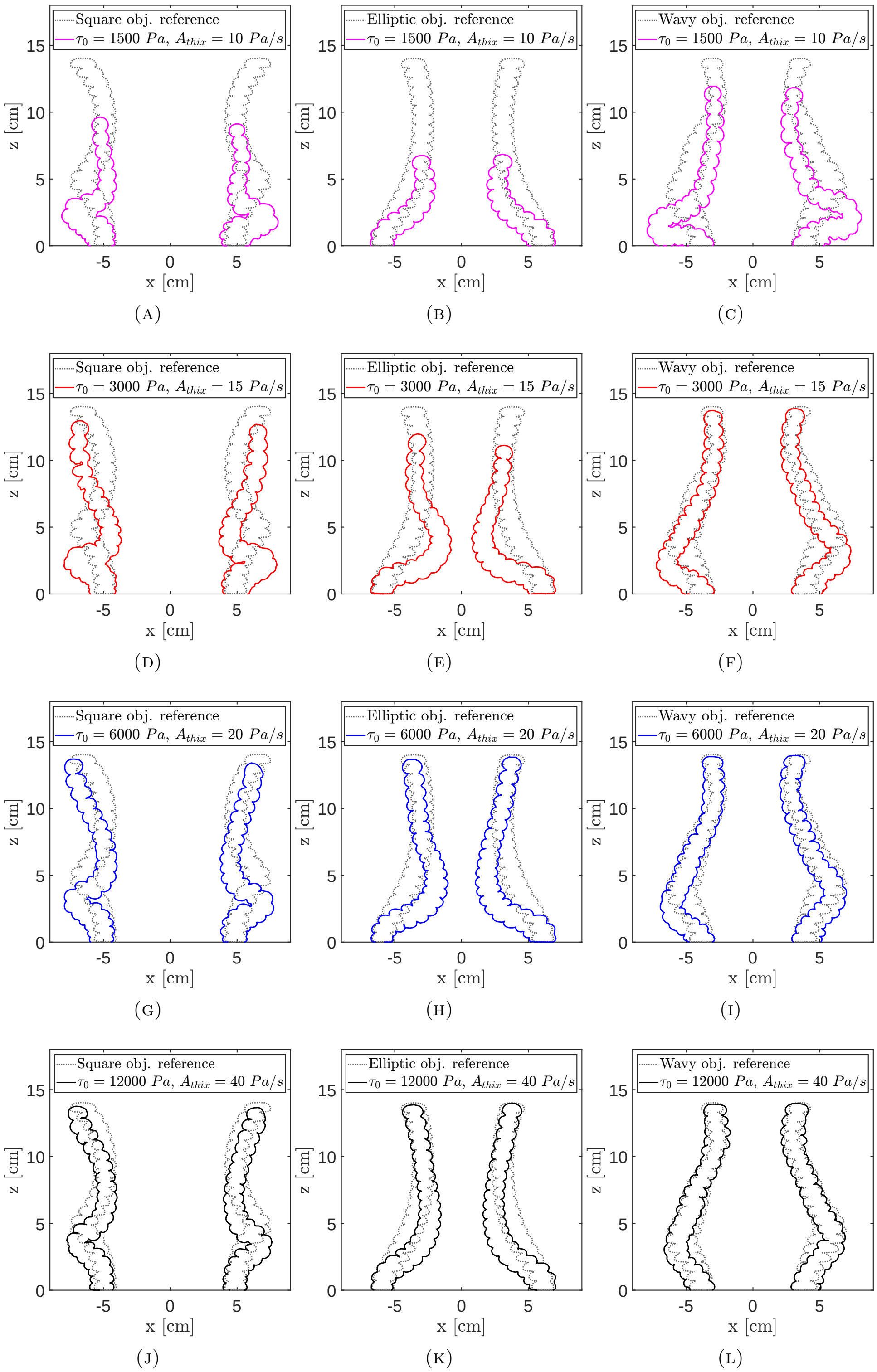

(A) (B) (C)

(D) (E) (F)

(G) (H) (I)

(J) (K) (L)

FIGURE 13. Comparison between reference and numerical cross-sections for the three objects when printed with different materials.

When the yield stress and structural build-up rate are increased to the values of material M2, a modest improvement in buildability is observed. The square object can be fully printed, but exhibits pronounced deformations (Figure 13-D), and the final height underestimates the target one by approximately 8.6%. The elliptic object sustains more layers than before, but collapses during the 18^{th} layer (Figure 13-E). Finally, the wavy object can be printed in full with material M2, though also with noticeable deviations from the target geometry (Figure 13-F), resulting in a relative height error of 1.5%.

A further increase in yield stress and structural build-up rate, as in material M3, enables completion of the printing process for all geometries, although appreciable deformation persists. The square object exhibits lateral displacements comparable to the layer width (Figure 13-G) and a vertical height error of 3.57%, highlighting how the overhangs introduced by twisting increase the difficulty of the process. The elliptic object remains prone to inward bending, resulting in a visibly distorted cross-section (Figure 13-H) and a vertical error of 1.89%. By contrast, the wavy object shows good agreement with the target geometry (Figure 13-I), with only limited residual vertical deformation of 0.61%, confirming its higher tolerance to moderate material performance.

The highest-performance material (M4) yields the best overall results across all objects, with printing successfully completed in every case. The square object, however, still exhibits significant lateral displacements, comparable to the nozzle width (Figure 13-J), and a vertical height error of 2.29 %, indicating that this geometry remains challenging even under favourable rheological conditions. The elliptic object shows improved performance, with a relative height error of 0.71 %, although minor inward deformation is still observed (Figure 13-K). The wavy object displays excellent agreement with the target geometry, with minimal distortions at curvature transitions (Figure 13-L) and a total relative height error of 0.5 %.

Results are reported in Table 2 in terms of the number of layers at collapse (n) or, in cases where all 20 layers are successfully printed, as the relative height error (expressed as a percentage):

$$e_h^{(\%)} = \frac{h_{\text{ref}} - h_{\text{sim}}}{h_{\text{ref}}} \times 100, \tag{30}$$

where $h_{\text{ref}} = n * h = 20 * 7\,\text{mm} = 140\,\text{mm}$ is the target reference height, and h_{sim} is the total height of the simulated object after deposition of the final layer. While the number of layers at collapse provides an indicator of buildability, the relative height error offers a quantitative measure of the geometric conformity of the fully printed object with respect to the intended design configuration.

Table 2. Virtual printing results for each material and geometry. Reported values are the number of layers at collapse (n) and for fully printed objects ($n = 20$), the relative height error e_h (%).

Material	Square	Elliptic	Wavy
M1	14 (-)	10 (-)	18 (-)
M2	20 (8.6%)	18 (-)	20 (1.50%)
M3	20 (3.57%)	20 (1.89%)	20 (0.61%)
M4	20 (2.29%)	20 (0.71%)	20 (0.50%)

Overall, these results demonstrate that increasing the static yield stress and the thixotropic build-up rate systematically enhances buildability. However, the required level of material performance is strongly modulated by geometric complexity. A concise summary of buildability limits and geometric conformity as functions of the static yield stress is reported in Table 3 for the different geometries. The table also includes numerically derived indications for optimal support placement to further improve geometric accuracy, as discussed in detail below.

Table 3. Summary of virtual printing results for different material properties across the complex objects.

	Square	Elliptic	Wavy
Stability threshold	$\tau_0 \geq 6000$ Pa	$\tau_0 \geq 6000$ Pa	$\tau_0 \geq 3000$ Pa
Geometrical conformity	never acceptable	$\tau_0 \geq 12000$ Pa	$\tau_0 \geq 6000$ Pa
Sand support	inside and outside	mainly inside	only outside

While the wavy object can be successfully printed with the intermediate material, the square and elliptic objects require substantially higher rheological properties to ensure both stability and acceptable geometric accuracy. Achieving such conditions may be challenging in practice, thereby motivating the adoption of auxiliary strategies.

One approach is to tailor the ink formulation in order to accelerate the fluid-to-solid phase transition. For cementitious materials, this can be accomplished by injecting accelerators or other chemical admixtures immediately upstream of the nozzle, as implemented in so-called two-component (2K) printing systems [47]. Polymeric materials are generally less affected by these constraints, as their thermally driven phase transition is typically much faster.

When modifying the material composition or setting kinetics is not feasible - as in the case of clays or cementitious materials printed using one-component (1K) systems - an alternative solution is the use of internal and/or external support strategies to enable stable printing of more demanding geometries. For cement- or clay-based materials, this commonly involves filling or surrounding the object with sand during printing. In this context, numerical analysis is particularly valuable, as it enables the identification of where support is most effective for each geometry. The resulting recommendations on optimal support placement, derived from the numerical simulations, are summarized in Table 3 and can substantially improve final print quality while relaxing the requirements on the static yield stress.

6. Conclusions.

This study demonstrates how high-fidelity, fluid-based simulations can be extended to complex, multi-layer 3D printing processes, including geometries with overhangs, twists, and height-varying cross-sections. Using the Particle Finite Element Method (PFEM), both extrusion and layer deposition are fully resolved without simplifying assumptions, enabling accurate representation of near-nozzle effects such as local pressure increases and yielding, and thereby providing high-fidelity predictions of geometric conformity and buildability.

Faithful reproduction of intricate toolpaths in this advanced framework is nontrivial. We therefore investigated the effects of toolpath discretization and time-step size on nozzle motion and developed two novel G-code optimization strategies - arc-length resampling and adaptive time step cutting - which ensure precise and efficient nozzle motion resolution, without globally reducing the simulation time step.

The approach was applied for modelling of complex parametric geometries, generated in Rhino 3D + Grasshopper and exported via G-code to the FEM environment. Simulations were performed for progressively increasing material performance, revealing how material behaviour and geometry jointly govern stability and shape fidelity, while also enabling informed decisions on ink formulation and the use of supports.

Overall, the framework retains its flexibility across a broad range of material classes - from polymers to clays and cementitious inks - and can be further extended to thermo-mechanical simulations, enabling high-fidelity modeling of thermoplastic or glass-based extrusion processes.

Acknowledgments. The first author is supported by the project "Material and Process Modelling for Lunar 3D Printing", CUP D47G25000060006, pursuant to Notice No. 47 of 20/02/2025 ('Decree for the recruitment of international post-doctoral researchers'), PNRR, Mission 4, Component 2, Investment 1.2, financed by the European Union - NextGeneration EU. This research was also partially supported by the Italian Ministry of University and Research through the project PRIN2022 DTWIX: development of Digital TWIns for multiphysics simulation of eXtreme events in civil engineering (PRIN DTWIX - 2022AL5MSN).

REFERENCES

[1] S. C. Altıparmak, V. A. Yardley, Z. Shi and J. Lin, Extrusion-based additive manufacturing technologies: State of the art and future perspectives, *J. Manuf. Process.*, **83** (2022), 607-636.

[2] B. Brenken, E. Barocio, A. Favaloro, V. Kunc and R. B. Pipes, Development and validation of extrusion deposition additive manufacturing process simulations, *Addit. Manuf.*, **25** (2019), 218-226.

[3] F. Brezzi and M. Fortin, *Mixed and Hybrid Finite Element Methods*, vol. 51, New York: Springer-Verlag, 1991.

[4] A. Cattenone, S. Morganti, G. Alaimo and F. Auricchio, Finite element analysis of additive manufacturing based on fused deposition modeling: Distortions prediction and comparison with experimental data, *J. Manuf. Sci. Eng.*, **141** (2019), 011010.

[5] M. L. Cerquaglia, D. Thomas, R. Boman, V. Terrapon and J.-P. Ponthot, A fully partitioned Lagrangian framework for FSI problems characterized by free surfaces, large solid deformations and displacements, and strong added-mass effects, *Comput. Methods Appl. Mech. Eng.*, **348** (2019), 409-442.

[6] F. Chirianni, G. Vairo and M. Marino, Development of process design tools for extrusion-based bioprinting: From numerical simulations to nomograms through reduced-order modeling, *Comput. Methods Appl. Mech. Eng.*, **419** (2024), 116685.

[7] R. Comminal, W. R. Leal da Silva, T. J. Andersen, H. Stang and J. Spangenberg, Modelling of 3D concrete printing based on computational fluid dynamics, *Cem. Concr. Res.*, **138** (2020), 106256.

[8] M. Cremonesi, A. Franci, S. Idelsohn and E. Oñate, A state of the art review of the particle finite element method (PFEM), *Arch. Comput. Methods Eng.*, **27** (2020), 1709-1735.

[9] N. Dhakal, X. Wang, C. Espejo, A. Morina and N. Emami, Impact of processing defects on microstructure, surface quality, and tribological performance in 3D printed polymers, *J. Mater. Res. Technol.*, **23** (2023), 1252-1272.

[10] J. Donea, A. Huerta, J.-P. Ponthot and A. Rodríguez-Ferran, Arbitrary Lagrangian–Eulerian methods, in *Encyclopedia of Computational Mechanics (eds. E. Stein, R. de Borst and T. J. Hughes)*, John Wiley & Sons, Ltd., (2017), 1-23.

[11] H. Edelsbrunner and E. P. Mücke, Three-dimensional alpha shapes, *ACM Trans. Graph.*, **13** (1994), 43-72.

[12] S. Février, E. Fernández, M. Lacroix, R. Boman and J.-P. Ponthot, Simulation of melt pool dynamics including vaporization using the particle finite element method, *Comput. Mech.*, **75** (2025), 1787-1815.

[13] A. Franci and M. Cremonesi, On the effect of standard PFEM remeshing on volume conservation in free-surface fluid flow problems, *Comput. Part. Mech.*, **4** (2017), 331-343.

[14] T. J. R. Hughes, L. P. Franca and M. Balestra, A new finite element formulation for computational fluid dynamics: V. Circumventing the Babuška-Brezzi condition: A stable Petrov-Galerkin formulation of the stokes problem accommodating equal-order interpolations, *Comput. Methods Appl. Mech. Eng.*, **59** (1986), 85-99.

[15] M. Manivel, M. Silva and R. Thompson, Iterative respacing of polygonal curves, *SN Comput. Sci.*, **3** (2022), 419.

[16] A. Montalti, P. Ferretti and G. M. Santi, From CAD to G-code: Strategies to minimizing errors in 3D printing process, *CIRP J. Manuf. Sci. Technol.*, **55** (2024), 62-70.

[17] D. H. F. R. Moreira, G. Avancini and R. A. K. Sanches, A monolithic PFEM-FEM approach for fluid–structure interaction with structural contact: Applications in engineering and biomechanics, *Comp. Part. Mech.*

[18] V. Nguyen-Van, B. Panda, G. Zhang, H. Nguyen-Xuan and P. Tran, Digital design computing and modelling for 3-D concrete printing, *Autom. Constr.*, **123** (2021), 103529.

[19] E. Oñate, A. Franci and J. M. Carbonell, A particle finite element method for analysis of industrial forming processes, *Comput. Mech.*, **54** (2014), 85-107.

[20] E. Oñate, S. R. Idelsohn, F. Del Pin and R. Aubry, The particle finite element method—An overview, *Int. J. Comput. Methods*, **1** (2004), 267-307.

[21] T. Ooms, G. Vantyghem, R. Van Coile and W. De Corte, A parametric modelling strategy for the numerical simulation of 3D concrete printing with complex geometries, *Addit. Manuf.*, **38** (2021), 101743.

[22] T. C. Papanastasiou, Flows of materials with yield, *J. Rheol.*, **31** (1987), 385-404.

[23] A. Perrot, A. Pierre, V. N. Nerella, R. J. M. Wolfs, E. Keita, S. A. O. Nair, N. Neithalath, N. Roussel and V. Mechtcherine, From analytical methods to numerical simulations: A process engineering toolbox for 3D concrete printing, *Cem. Concr. Compos.*, **122** (2021), 104164.

[24] A. Quarteroni, *Numerical Models for Differential Problems*, Springer Milan, 2014.

[25] N. Ramos, C. Mittermeier and J. Kiendl, Efficient simulation of the heat transfer in fused filament fabrication, *J. Manuf. Process.*, **94** (2023), 550-563.

[26] J. Reinold, V. N. Nerella, V. Mechtcherine and G. Meschke, Extrusion process simulation and layer shape prediction during 3D-concrete-printing using the Particle Finite Element Method, *Autom. Constr.*, **136** (2022), 104173.

[27] I. Rivet, N. Dialami, M. Cervera, M. Chiumenti and Q. Valverde, Mechanical analysis and optimized performance of G-code driven material extrusion components, *Addit. Manuf.*, **61** (2023), 103348.

[28] G. Rizzieri, D. Bos, R. Wolfs, L. Ferrara and M. Cremonesi, A unified fluid-solid elasto-viscoplastic finite element model for the simulation of 3D concrete printing across process scales, *Comput. Methods Appl. Mech. Eng.*, (2026).

[29] G. Rizzieri, M. Cremonesi and L. Ferrara, A 2D numerical model of 3D concrete printing including thixotropy, *Mater. Today*, (2023).

[30] G. Rizzieri, M. Cremonesi and L. Ferrara, Challenging the limits of fluid FEM modelling in 3D concrete printing, in *D. Lowke, N. Freund, D. Böhler and F. Herding (eds), Fourth RILEM International Conference on Concrete and Digital Fabrication*, Springer Nature Switzerland, Cham., (2024), 482-489.

[31] G. Rizzieri, L. Ferrara and M. Cremonesi, Numerical simulation of the extrusion and layer deposition processes in 3D concrete printing with the particle finite element method, *Comput. Mech.*, **73** (2024), 277-295.

[32] G. Rizzieri, L. Ferrara and M. Cremonesi, Simulation of viscoelastic free-surface flows with the Particle Finite Element Method, *Comput. Part. Mech.*, **11** (2024), 2043-2067.

[33] G. Rizzieri, L. Ferrara and M. Cremonesi, A partitioned Lagrangian finite element approach for the simulation of viscoelastic and elasto-viscoplastic free-surface flows, *Comput. Methods Appl. Mech. Eng.*, **443** (2025), 118071.

[34] G. Rizzieri, S. Meni, M. Cremonesi and L. Ferrara, A Particle Finite Element Method for investigating the influence of material and process parameters in 3D Concrete Printing, *Comput. Struct.*, **316** (2025), 107883.

[35] N. Roussel, A thixotropy model for fresh fluid concretes: Theory, validation and applications, *Cem. Concr. Res.*, **36** (2006), 1797-1806.

[36] N. Roussel, G. Ovarlez, S. Garrault and C. Brumaud, The origins of thixotropy of fresh cement pastes, *Cem. Concr. Res.*, **42** (2012), 148-157.

[37] J. Rymeš, J. Cervenka and L. Jendele, Material Modelling and simulation of 3D concrete printing process, in *Proceedings of the 11th International Conference on Fracture Mechanics of Concrete and Concrete Structures*, IA-FraMCoS, 2023.

[38] F. Salazar, J. Irazábal, A. Larese and E. Oñate, Numerical modelling of landslide-generated waves with the particle finite element method (PFEM) and a non-Newtonian flow model, *Int. J. Numer. Anal. Meth. Geomech.*, **40** (2016), 809-826.

[39] A. A. Samy, A. Golbang, E. Harkin-Jones, E. Archer, D. Tormey and A. McIlhagger, Finite element analysis of residual stress and warpage in a 3D printed semi-crystalline polymer: Effect of ambient temperature and nozzle speed, *J. Manuf. Process.*, **70** (2021), 389-399.

[40] O. Sandin, P. Larour, J. M. Rodríguez, S. Parareda, S. Hammarberg, J. Kajberg and D. Casellas, Numerical modelling of shear cutting in complex phase high strength steel sheets: A comprehensive study using the particle finite element method, *Finite Elem. Anal. Des.*, **246** (2025), 104331.

[41] M. Schewe, I. Noll, T. Bartel and A. Menzel, Towards the simulation of metal deposition with the particle finite element method and a phase transformation model, *Comput. Methods Appl. Mech. Eng.*, **437** (2025), 117730.

[42] M. P. Serdeczny, R. Comminal, D. B. Pedersen and J. Spangenberg, Experimental validation of a numerical model for the strand shape in material extrusion additive manufacturing, *Addit. Manuf.*, **24** (2018), 145-153.

[43] H. Si, TetGen, a Delaunay-based quality tetrahedral mesh generator, *ACM Trans. Math. Softw.*, **41** (2015), Art. 11, 36 pp.

[44] J. Spangenberg, W. R. L. da Silva, R. Comminal, M. T. Mollah, T. J. Andersen and H. Stang, Numerical simulation of multi-layer 3D concrete printing, *RILEM Technical Letters*, **6** (2021), 119-123.

[45] T. E. Tezduyar, S. Mittal, S. E. Ray and R. Shih, Incompressible flow computations with stabilized bilinear and linear equal-order-interpolation velocity-pressure elements, *Comput. Methods Appl. Mech. Eng.*, **95** (1992), 221-242.

[46] Z. Wang and D. E. Smith, Finite element modelling of fully-coupled flow/fiber-orientation effects in polymer composite deposition additive manufacturing nozzle-extrudate flow, *Compos. B: Eng.*, **219** (2021), 108811.

[47] T. Wangler, Y. Tao, A. Das, M. Mahmoudi, S. Gürel and R. J. Flatt, Aluminate 2K systems in digital concrete: Process, design, chemistry, and outlook, *Cem. Concr. Res.*, **185** (2024), 107644.

[48] R. J. M. Wolfs, F. P. Bos and T. A. M. Salet, Early age mechanical behaviour of 3D printed concrete: Numerical modelling and experimental testing, *Cem. Concr. Res.*, **106** (2018), 103-116.

[49] R. J. M. Wolfs and A. S. J. Suiker, Structural failure during extrusion-based 3D printing processes, *Int. J. Adv. Manuf. Technol.*, **104** (2019), 565-584.

[50] H. Xia, J. Lu and G. Tryggvason, A numerical study of the effect of viscoelastic stresses in fused filament fabrication, *Comput. Methods Appl. Mech. Eng.*, **346** (2019), 242-259.

[51] X. Xu, H. Ren, S. Chen, X. Luo, F. Zhao and Y. Xiong, Review on melt flow simulations for thermoplastics and their fiber reinforced composites in fused deposition modeling, *J. Manuf. Process.*, **92** (2023), 272-286.

[52] H. Zhang, F. Ye, F. Chen, W. Yuan and W. Yan, Numerical investigation on the viscoelastic polymer flow in material extrusion additive manufacturing, *Addit. Manuf.*, **81** (2024), 103992.

Received February 3, 2026; revised March 6, 2026.